metals

MDPI

Article

A Novel Non-Equiatomic $(W_{35}Ta_{35}Mo_{15}Nb_{15})_{95}Ni_5$ Refractory High Entropy Alloy with High Density Fabricated by Powder Metallurgical Process

Bohua Duan, Yingrui Yu, Xinli Liu *, Dezhi Wang and Zhuangzhi Wu

School of Materials Science and Engineering, Central South University, Changsha 410083, China; dbh72@163.com (B.D.); yyr021189@163.com (Y.Y.); dzwang@csu.edu.cn (D.W.); zwu2012@csu.edu.cn (Z.W.)

* Correspondence: liuxinli@csu.edu.cn

Received: 10 October 2020; Accepted: 25 October 2020; Published: 29 October 2020

Abstract: A non-equiatomic refractory high entropy alloy (RHEA), $(W_{35}Ta_{35}Mo_{15}Nb_{15})_{95}Ni_5$ with high density of 14.55 g/cm^3 was fabricated by powder metallurgical process of mechanical alloying (MA) and spark plasma sintering (SPS). The mechanical alloying behavior of the metallic powders was studied systematically, and the microstructure and phase composition for both the powders and alloys were analyzed. Results show that the crystal consists of the primary solid solution and marginal oxide inclusion ($Nb_{5.7}Ni_4Ta_{2.3}O_2$). In addition, the maximum strength, yield strength and fracture strain are, 2562 MPa, 2128 MPa, 8.16%, respectively.

Keywords: refractory; high entropy alloy; mechanical alloying; phase transformation; mechanical properties

1. Introduction

With the rapid development of advanced science and technology in the fields of armor piercing projectile, counter weight balance, radiation shields, shaped charge liner in ordnance industry and high-density gradient materials in dynamic high-pressure physics, the demand for materials with high density has boosted wide study on heavy metals and alloys [1]. Recently, a novel type of advanced refractory metallic alloys, refractory high entropy alloys, have been regarded as a potential candidate. High entropy alloy is a kind of alloy with high entropy of more than 1.61 R (when the alloys have 5 components). The different atoms with different bonding energy and crystal structure make the crystal lattice complex, and solute phases lead to severe lattice distortion in high entropy alloy (HEAs). These distortions are proposed to be more severe than in conventional alloys. The diffusion of atoms in HEAs mainly occurs via the vacancy diffusion mechanism. Due to the different melting points of the components, the element with high migration rate will preferentially diffuse to the vacancies. However, different atoms in HEAs have different bonding energies. Once atoms fill in vacancy, the energy of the system will decrease or increase. As a result, compared to the conventional alloys, the atomic diffusion and phase transformation processes in HEAs are relatively slow. This is called the sluggish diffusion effect in HEAs [2]. Refractory high entropy alloys (RHEAs) possess many excellent properties, such as high strength and hardness, and excellent creep resistance, due to its lattice distortion effect and sluggish diffusion effect [2]. Unlike conventional alloys with one or two major elements, RHEAs are generally made up of multiple principle refractory elements (≥5), such as Cr, W, Ta, Mo, Nb, Ti, V, Zr, Hf, and other elements of Al, Ni, Co, Si, C and N [3] in equimolar or near-equimolar proportions (5–35 at%). For the moment, the HEAs was recognized consisting of at least four major metallic elements in non-equimolar ratios (5–35 at%). The most common RHEAs include WTaMoNb, HfNbTaTiZr, NbTiVZr, AlNbTiV and CrMoVW, which have received extensive attention due to the easy way to tailor the phase stability and phase microstructure to enhance mechanical properties [4].

Up to now, various fabrication methods have been adopted to manufacture the HEAs, such as vacuum arc-melting and casting, sintering, magnetron sputtering and laser cladding. Among these methods, vacuum arc-melting and casting is generally applied to product bulk HEAs. However, the defects such as segregation and inhomogeneous dendritic microstructures generally exist in HEAs which are prepared by casting, and may be harmful to mechanical properties [5]. A few HEA systems were manufactured by mechanical alloying (MA) process [6]. HEA powders produced by MA process exhibit many advantages, such as more homogeneous morphologies and precise composition control. However, the milling time which achieves alloying is overwhelmingly long [6,7]. Some researches described appropriate addition of Ni can reduce reaction energy barrier and significantly accelerate the reaction among brittle phase during MA process [8]. Spark plasma sintering (SPS) technique is a new technology for preparing materials, which has the distinctive characteristics of fast heating speed, short sintering time, controllable structure, energy saving and environmental protection, and can be used to prepare metals materials, ceramic materials and composite materials, et al. The MA and SPS processes can exhibit some significant advantages, such as lower processing temperature, finer grain and more homogeneous microstructure, and excellent mechanical properties of the bulk alloys [7,9].

Our motivation is to develop a HEA material with high strength, closely related to the well-known refractory WTaMoNb HEA [10]. We design $(W_{35}Ta_{35}Mo_{15}Nb_{15})_{95}Ni_5$ RHEA with high theoretical density of 15.12 g/cm^3 via regulating constituent molar ratio and addition of fcc-Ni to accelerate the alloying process. Given the high melting temperature of refractory elements and the traits of fabrication methods, we will adopt powder metallurgical processes to fabricate bulk RHEA.

In this study, a novel $(W_{35}Ta_{35}Mo_{15}Nb_{15})_{95}Ni_5$ RHEA is fabricated by mechanical alloying and spark plasma sintering process. The alloying behavior, phase compositions were analyzed, and the mechanical property was also studied.

2. Materials and Methods

2.1. Synthesis of RHEA

The schematically preparation process was presented in Figure 1. The first process is the synthesis of $(W_{35}Ta_{35}Mo_{15}Nb_{15})_{95}Ni_5$ refractory high entropy alloy (RHEA) powders by mechanical alloying (MA). The RHEA powders were prepared by high-energy ball milling (YXQM-4L, MITR Co., Ltd., Changsha, China) of elemental W, Ta, Mo, Nb and Ni powders, and all the powders were purchased from Beijing Xingrongyuan Technology Co., LTD, China with purity of more than 99.9% and diameter of less than 5 μm. The W, Ta, Mo, Nb and Ni powders with atomic ratio of 33.25:33.25:14.25:14.25:5 were placed in a stainless-steel tank filled with tungsten carbide balls. The MA process was carried out in a high-purity argon gas atmosphere to prevent oxidation with a high-energy planetary ball mill at 300 rpm, and a ball to powder weight ratio of 10:1. To analyze the MA behavior of the HEA powders, powders were sampled after 0.25, 2, 4, 10 and 12 h of milling. All of these procedures were carried out in a glove box filled with high-purity argon gas to prevent oxidation of the HEA powders. In order to ensure the metallic powders fully alloying, the powders ball milled for 12 h were selected to sinter via spark plasma sintering (SPS, HP D25, FCT Systeme GmbH, Rauenstein, Germany) at pressure of 30 MPa under vacuum. The metallic powders were placed in the carbon mold, and then the upper and lower carbon die punches are put into the carbon mold. The SPS process are carried out applying a specific sintering power resource and pressing pressure to the sintered powder. The powders were heated to 420 °C within 2 min, and from 420 °C to final temperature of 1700 °C at a heating rate of 100 °C min^{-1}, followed by 10 min of holding time at the sintering temperature.

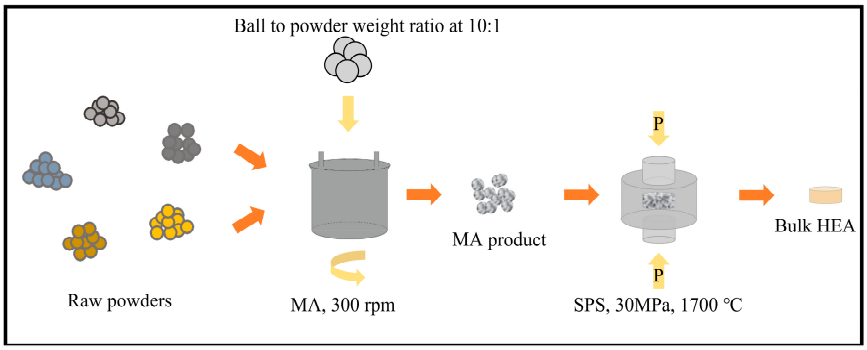

Figure 1. Schematic demonstration of the processing route adopted for the fabrication of $(W_{35}Ta_{35}Mo_{15}Nb_{15})_{95}Ni_5$ high entropy alloy (HEA).

2.2. Characterization

The particle size distribution of the HEA powder was determined by a laser particle size analyzer (MALVERN, MICRO-PLUS, UK) using water as dispersant. The crystal structure of the alloyed powders and sintered bulk specimen were identified by X-ray diffraction (XRD, Rigaku, D/max 2550VB, Japan, scan rate of 8 deg min^{-1}, scan-step size of 0.02 deg, scan angle range of 20–90 deg) using CuK_α radiation at 40 KV and 450 mA. The microstructure and alloying component distribution of the mechanically alloyed HEA powder were analyzed by transmission electron microscopy (TEM, JEM-2100F, JEOL, Tokyo, Japan). The microstructure of the $(W_{35}Ta_{35}Mo_{15}Nb_{15})_{95}Ni_5$ HEA was characterized by field emission scanning electron microscopy (SEM, NOVATM NanoSEM230, FEI, Eindhoven, the Neitherland) equipped with the energy dispersive (EDS, GENESIS60S). The secondary electron (SE) imaging mode was used to observe the morphology of the samples. The back-scattered electron (BSE) imaging mode was used to distinguish the different phases of the microstructure. The alloying element distribution was measured by electron probe microanalysis (EPMA, JXA-8230, JEOR, Tokyo, Japan) with back-scattered mode. Metallographic specimens were prepared by grinding, polishing and chemical etching in an aqueous solution (m_{KOH}:$m_{k3FeCN6}$:m_{H2O} = 1:1:18). The density of the $(W_{35}Ta_{35}Mo_{15}Nb_{15})_{95}Ni_5$ HEA was determined using Archimedes' method with distilled water. Compressive stress–strain testing was carried out in universal testing machine (3369, INSTRON, Bosto, MA, USA) with cylindrical specimens (Φ 6 mm × 8 mm) at an engineering strain rate of 2 mm min^{-1} at room temperature. The representative data was obtained by averaging three values of the test results.

3. Results and Discussion

3.1. Alloying Process

Figure 2 depicts the XRD patterns of $(W_{35}Ta_{35}Mo_{15}Nb_{15})_{95}Ni_5$ HEA powders after different milling time. The mixed powders after 0.25 h of milling contains diffraction patterns of all constituent elements, while the least atomic weight leaded to that the characteristic peak of intensities of Ni were relatively lower than those of the other elements, because the peak intensities of each element are related to the atomic number of the constituents [11]. The intensities of the diffraction peaks declined sharply and the characteristic peak of Ni disappeared after 2 h of milling, as shown in Figure 2a, which recommends sufficient dissolution of Ni. With the milling time prolonged to 4 h, the characteristic peaks of Mo and Nb clearly merged into the peaks of Ta and W. After 10 h of milling, the constituent elements peaks are no longer observed, and it is obvious that four new diffraction peaks appearing at 2θ ≈ 39.94°, 57.78°, 72.56° and 86.19° are quite well with (110), (200), (211) and (220) planes of a simple solid solution structure. The declined and broadened diffraction peaks are largely ascribed to the refinement of the grain size and the increment of the lattice strain. All diffraction peaks are consistent with a single bcc phase. The minimum alloying time for $(W_{35}Ta_{35}Mo_{15}Nb_{15})_{95}Ni_5$ RHEA powders is shorter than that of some common RHEAs [6,7] powders may due to the addition of Ni.

In fact, the solid solution sequence of the alloying elements is closely related to their melting points [12]. Generally, elements with lower melting points would have higher alloying rate than that with higher melting points. From what has been discussed above, we can draw a conclusion that the mechanical alloying procedure is that the decrease in the peak intensity, broadening and merging of the diffraction peaks and the subsequent disappearance, which is due to the factors: crystal size refinement, lattice strain increasement and reduced crystallinity [13].

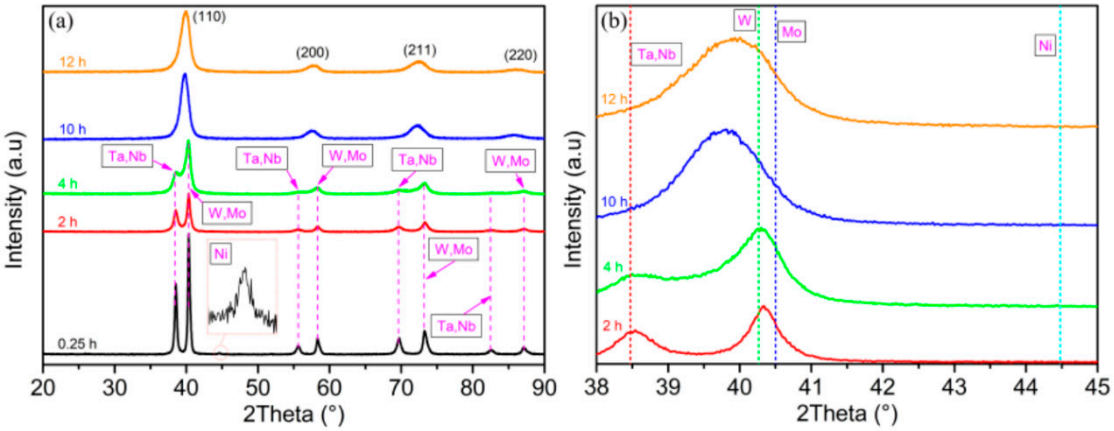

Figure 2. (**a**) XRD patterns of $(W_{35}Ta_{35}Mo_{15}Nb_{15})_{95}Ni_5$ HEA powders after different milling time, and (**b**) magnified XRD patterns of the 2, 4, 10 and 12 h-milled powders at 2θ range of 38–45°.

The breadth of the diffraction peak is a combination of both instrument and sample dependent effects. To eliminate instrumental contributions, it is necessary to obtain a diffraction pattern from the line broadening of a standard material such as silicon powders that are annealed at 1100 °C for 30 min to determine the instrumental broadening. The instrumental-corrected broadening β_D corresponding to the diffraction peak of $(W_{35}Ta_{35}Mo_{15}Nb_{15})_{95}Ni_5$ was evaluated using the relation as follows [14]:

$$\beta_D{}^2 = \beta^2{}_{measured} - \beta^2{}_{instrumental} \quad (1)$$

The grain size was determined according to the Scherrer equation:

$$D = \frac{k\lambda}{\beta_D \cos\theta} \quad (2)$$

where D is the grain size in nanometers, λ is the wavelength of the radiation (0.154056 nm for CuK_α radiation). k is a constant equal to 0.94, β_D is the peak width at half-maximum intensity and θ is the peak position. The lattice strain of HEAs were calculated according to the Williamson–Hall equation [15]:

$$\beta \cos\theta = \frac{k\lambda}{D} + \varepsilon \sin\theta \quad (3)$$

where β is assumed to be β_D, ε is the lattice strain.

The dislocation density ρ was calculated using the following equation [16]:

$$\rho = \frac{2\sqrt{3}\varepsilon}{Db} \quad (4)$$

where ε, D and b are lattice strain, grain size and Burgers vector, respectively. b is equal to $\frac{\sqrt{3}}{2}a$ (a is the lattice parameter determined in the means of the Nelson-Riley approach with the weighting function $1/2(\cot^2\theta + \cos\theta\cot\theta)$ [17]) for a bcc structure, ε and D are calculated from the XRD patterns based on Equation (2).

Figure 3a shows grain size and lattice strain under different milling duration. By and large, with increasing milling time, the grain size become lower, while the lattice strain become larger. As shown, the grain size refined with a large margin to 18.1 nm after 10 h milling time and then slightly decreases to 16.3 nm after 12 h MA, along with the lattice strain increases to 5.87% from 4.15%. Finally, the grain sizes and lattice strain of the powders reaches a dynamic balance after milling for 10 h. The dislocation density gradually become larger with prolonged milling time according to the Equation (4). The morphology and particle size distribution of the HEA powders obtained after 12 h ball milling treatment is shown in Figure 3b. The mechanically alloyed powders with mean size of 5.29 μm are made up of a large amount of refined powders and relatively much larger powders. The approximate spherical morphologies of the HEA powders demonstrate great fluidity, promote the relative high density of as-sintered bulk materials. We choose the powders with milling time of 12 h to sinter, which has been completely alloyed.

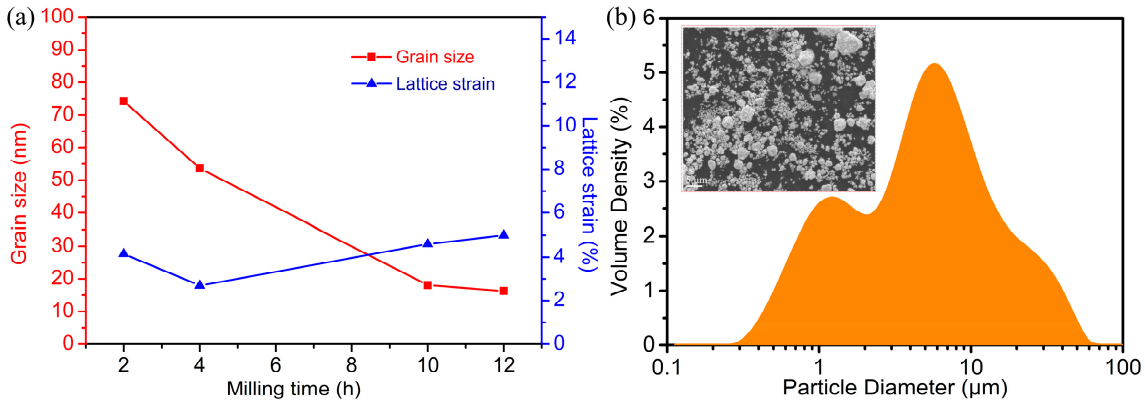

Figure 3. (**a**) Grain size and lattice strain for the powders at different milling time, (**b**) the morphology and the powder particle size distribution curve of the 12 h-milled powders.

Figure 4 is the high-resolution TEM (HRTEM) image of HEA powders after 12 h milling, and fast Fourier transformation images from the region is shown in the inset. The interplanar distance is 0.23 nm determined by the HRTEM image. Scanning TEM-energy dispersive X-ray analysis (STEM-EDX) was also conducted to qualitatively verify the elemental distribution in HEA powder. Figure 5 clearly illustrates that the element of the $(W_{35}Ta_{35}Mo_{15}Nb_{15})_{95}Ni_5$ RHEA are uniformly dispersed.

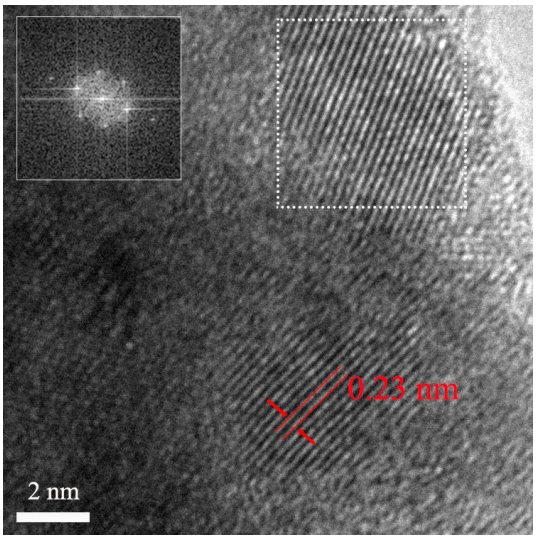

Figure 4. HRTEM image of the HEA powder after 12 h milling and fast Fourier transformation image.

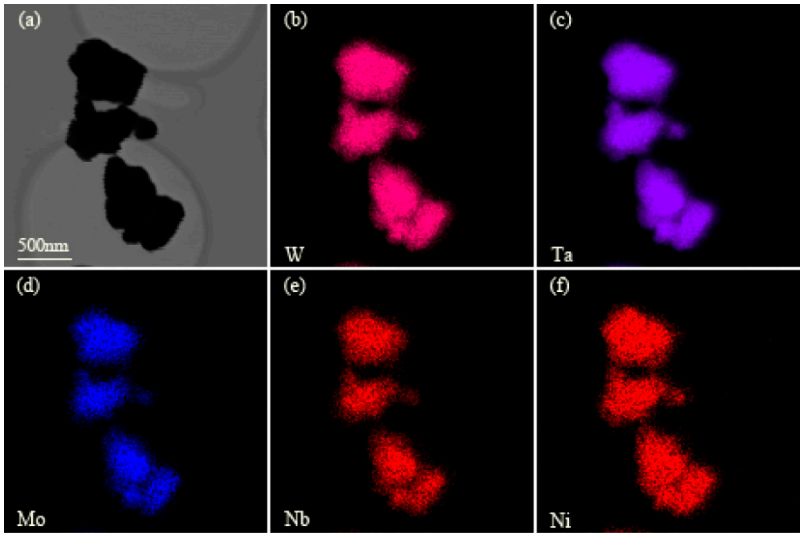

Figure 5. TEM image and corresponding EDX map for each component of HEA powder after 12 h milling, (**a**)TEM image, (**b**–**f**) EDS mappings of W, Ta, Mo, Nb and Ni, respectively.

3.2. *Phase and Microstructure of the Bulk RHEA*

The crystal structure and phase analysis were investigated by XRD. Figure 6 shows the XRD pattern of the $(W_{35}Ta_{35}Mo_{15}Nb_{15})_{95}Ni_5$ bulk alloy consolidated by SPS. The pattern of the powders milled for 12 h is also presented for comparison. The theoretical crystal lattice parameter a_{mix} of the bcc solid solution in non-equiatomic $(W_{35}Ta_{35}Mo_{15}Nb_{15})_{95}Ni_5$ RHEA is calculated to be a_{mix} = 0.324 nm using the rule of mixtures, while the lattice parameter of as-sintered bulk RHEA determined by the XRD is 0.320 nm based on Nelson-Riley approach [17]. It can be concluded that the calculated value for the $(W_{35}Ta_{35}Mo_{15}Nb_{15})_{95}Ni_5$ RHEA is very close to the experimental result. Compared with the XRD pattern of 12 h-milled powder, peaks shift can be clearly observed for the as-sintered bulk. The peaks position transfer toward lower Bragg angle (2θ), indicating that the lattice parameter of as-sintered bulk RHEA is larger than that of 12 h-milled RHEA powder (a = 0.319 nm). The XRD patterns indicate that the bulk specimens exhibit a single bcc structure. Besides, the minor diffraction peaks in the XRD pattern closely matched with cubic $Nb_{5.7}Ni_4Ta_{2.3}O_2$ (PDF#82-0947). A few diffraction peaks intensity is inconsistent with that of the PDF card may because the intensities of the XRD diffraction peaks decreases due to the appeared extremely refined oxide inclusion. As shown in Figure 6, the predominant crystal structure for both $(W_{35}Ta_{35}Mo_{15}Nb_{15})_{95}Ni_5$ bulk sample and powders is a single-phase solid solution with bcc structure, which demonstrates there was no phase decomposition during the SPS process.

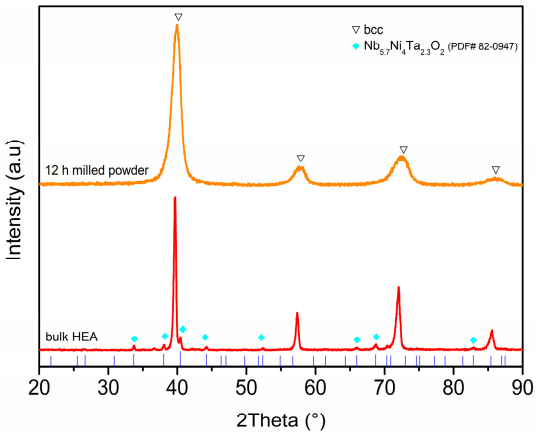

Figure 6. XRD patterns of HEA powders after milling for 12 h and bulk specimen sintered at 1700 °C.

Generally, the formation of metallic materials decides their physical and chemical properties. High entropy alloys are deemed as a kind of novel metallic materials, thus the phase structure and stability prediction have great significance for the design and application of these types of material. Since the concept of HEA was introduced by Yeh et al. [18], many literatures have reported physical parameters to predict the phase structure and stability of HEAs. Especially, the parameters δ (the atomic size difference) and Ω (a thermodynamic parameter) that were proposed [19] can predict the structure and stability of HEA. The parameter δ is defined as:

$$\delta = \sqrt{\sum_{i=1}^{n} c_i \left(1 - \frac{ri}{\bar{r}}\right)^2} \quad (5)$$

where c_i is the atomic fraction of the ith element, r_i is the atomic radius of the ith element and $\bar{r}$ is the average atomic radius, which is calculated by $\bar{r} = \sum_{i=1}^{n} c_i r_i$.

The other parameter (Ω) is defined as:

$$\Omega = \frac{T_m \Delta S_{mix}}{|\Delta H_{mix}|} \quad (6)$$

where T_m is melting point calculated as weighted average of the constituting elements, ΔS_{mix} is the entropy of mixing for HEAs, which is calculated by $\Delta S_{mix} = -R \sum_{i=1}^{n} c_i \ln c_i$ and ΔH_{mix} is the enthalpy of mixing of HEAs, which is calculated by $\Delta H_{mix} = \sum_{i=1, i \neq j}^{n} 4\Delta H_{mix}{}^{AB} c_i c_j$. According to Yang [19], as $\delta \leq 6.6\%$ and $\Omega \geq 1.1$, a stable, solid solution phase is constructed in a HEA system.

The literature has proposed another important parameter [20], the valence electron concentration (*VEC*). *VEC* is calculated by:

$$VEC = \sum_{i=1}^{n} c_i (VEC)_i \quad (7)$$

where $(VEC)_i$ is the *VEC* for the ith alloying element. Guo et al. [20] criticized that a low *VEC* (<6.87) is partial to sole bcc structure's solid solution phase, whereas a high *VEC* (≥8) favors sole solid solution phase with fcc structure. When $6.87 \leq VEC < 8$, the mixture of bcc and fcc solid solution phase is displayed.

According to the Equations (5)–(7), the calculated values of δ, $\Omega$and *VEC* for the $(W_{35}Ta_{35}Mo_{15}Nb_{15})_{95}Ni_5$ HEA are 3.27%, 4.16 and 5.73 respectively. Hence, the formation of the current HEA is supposed to be a formation of single-phase solid solution with bcc structure. Our experimental results coincided exactly with the prediction.

Figure 7a shows the SEM image of the as-sintered $(W_{35}Ta_{35}Mo_{15}Nb_{15})_{95}Ni_5$ HEA. Likewise, the back-scatter electron imaging mode was utilized to distinguish the different phases of the bulk HEA as shown in Figure 7b. It suggests that the $(W_{35}Ta_{35}Mo_{15}Nb_{15})_{95}Ni_5$ HEA is composed of a light gray matrix and dark gray inclusion. We adopt SEM-EDS to determine chemical components in region A and region B. The EDS results are presented in Figure 7c,d. The EDS analysis result presents the region B were enriched in Ta, Nb and O, and had a much higher Ni content than region A, while the W, Mo elements in region B are deficient.

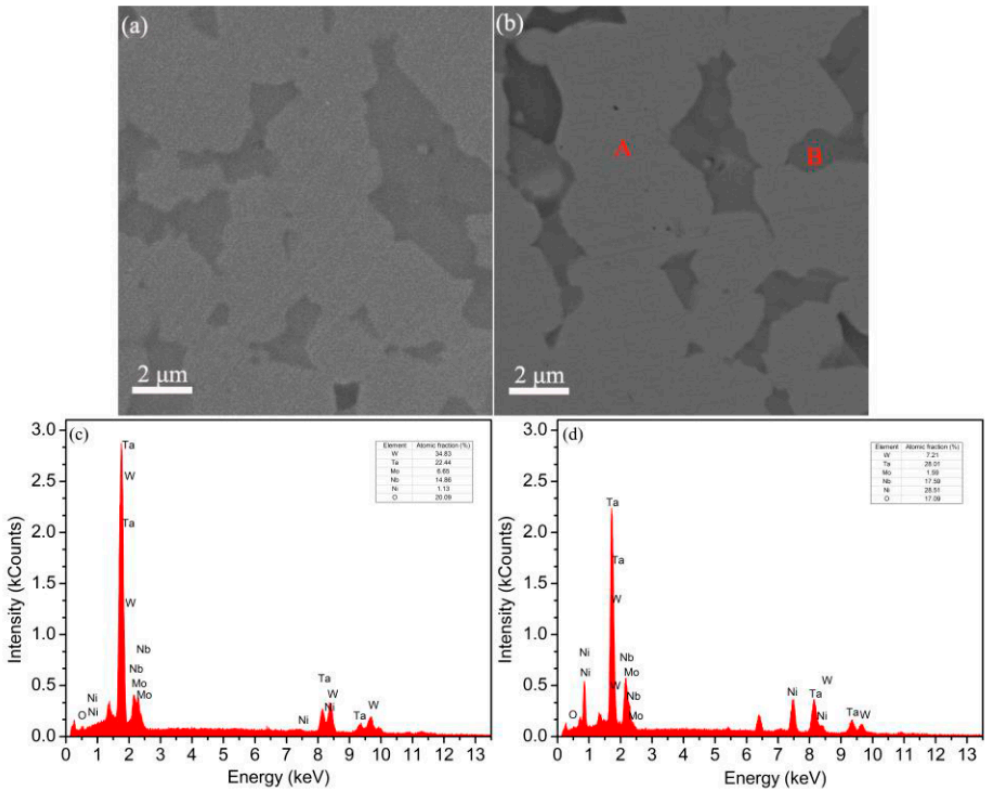

Figure 7. SEM image of the bulk $(W_{35}Ta_{35}Mo_{15}Nb_{15})_{95}Ni_5$ RHEA (**a**,**b**) with secondary electron and back-scattering electron mode, respectively, and EDS analysis of (**c**) region A and (**d**) region B marked in (**b**).

In order to further analyze the composition of the second phase in the bulk alloy, the back-scatter electron imaging mode and corresponding EDS-mapping were used to measure the distribution of the alloying elements in inclusion and matrix. The EDS-mapping analysis results are shown in Figure 8. The distribution of Ta, Nb elements was homogeneous in the HEA, whereas, the distribution of W, Mo, Ni elements were inhomogeneous. The light matrix is enriched in W, Mo and the distribution of W, Mo elements are homogeneous, but in the dark gray region are deficient. The dark gray region is enriched in Ni element, but in the light grey matrix were deficient. These results are consistent with the XRD analysis that the dark gray oxide inclusion should be $Nb_{5.7}Ni_4Ta_{2.3}O_2$ phase. The microstructure and element distribution of the alloy was further confirmed by EPMA. Figure 9 presents the EPMA mapping of alloying elements of the $(W_{35}Ta_{35}Mo_{15}Nb_{15})_{95}Ni_5$ HEA. As can be seen, alloying components Ni, Nb and Ta content is rich, while W and Mo are extremely minor in the region demonstrated by yellow circle. Thus, the EPMA analysis agrees with the XRD and the SEM results.

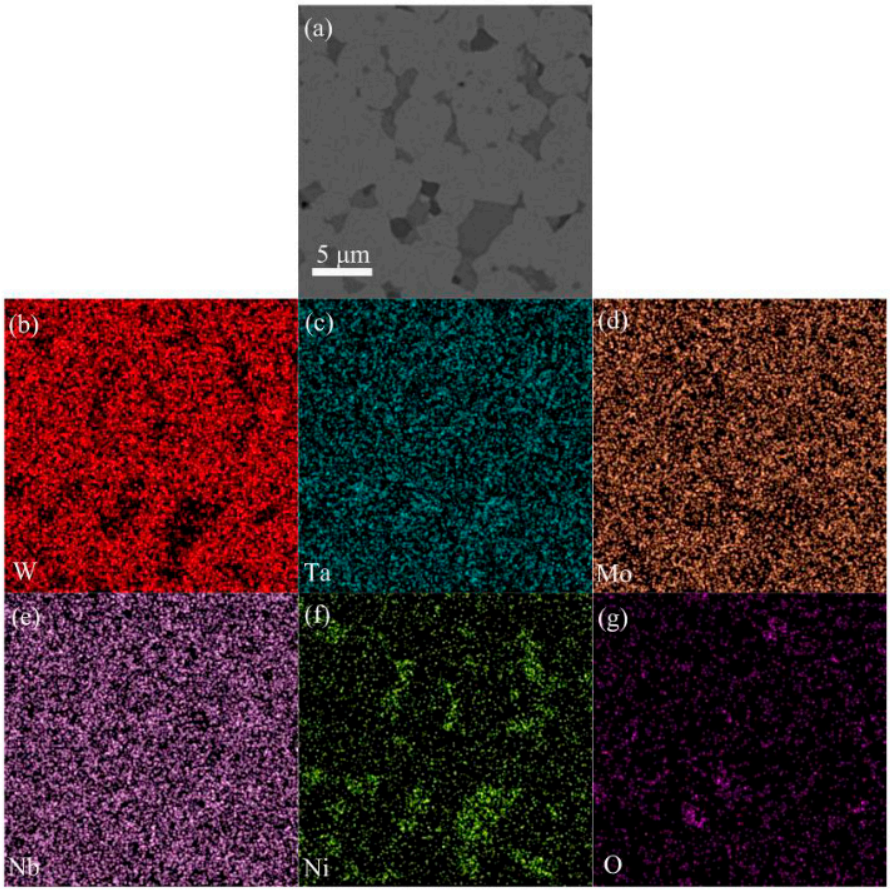

Figure 8. SEM-BSE image and corresponding EDS map for each component of $(W_{35}Ta_{35}Mo_{15}Nb_{15})_{95}Ni_5$ HEA bulk specimen, (**a**) SEM image, (**b**–**g**) EDS mappings of W, Ta, Mo, Nb, Ni and O respectively.

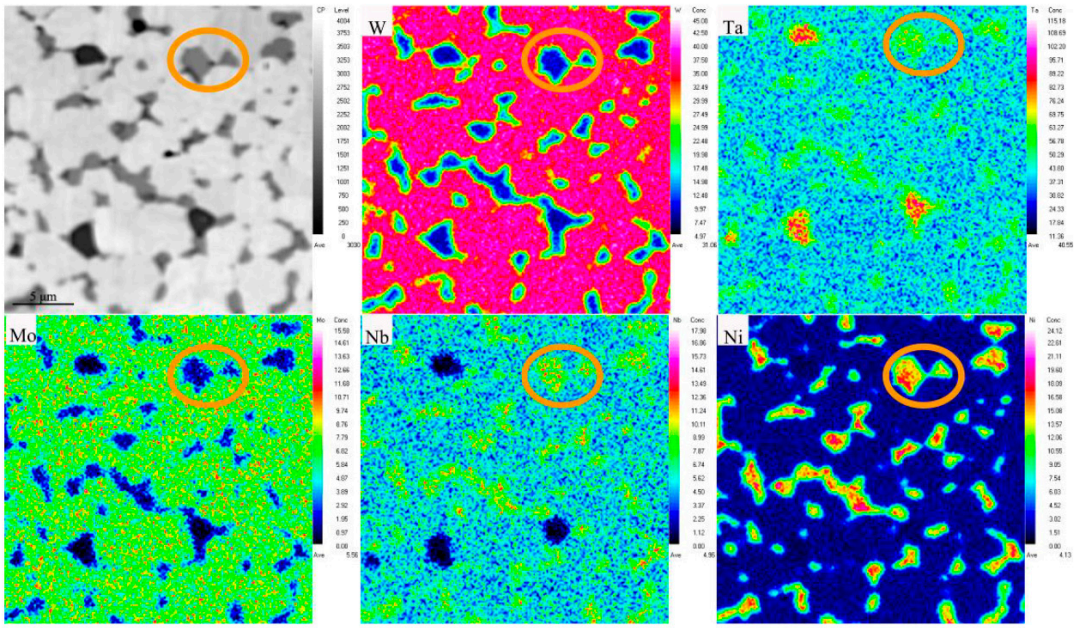

Figure 9. The EPMA-BSE image and the related mapping of alloying elements of the $(W_{35}Ta_{35}Mo_{15}Nb_{15})_{95}Ni_5$ HEA.

Figure 10a shows the microstructure of the $(W_{35}Ta_{35}Mo_{15}Nb_{15})_{95}Ni_5$ HEA bulk after chemical etching. The bulk materials via powder metallurgical process have a lot of pores as marked by red arrows. From the image, we can see that a large amount of inclusion marked by yellow arrows, are uniformly dispersed in the grain boundaries of the matrix combing with Figure 7b. We can clearly observe the grain marked by red dotted line, and the grain size of the bulk HEA was also measured from Figure 10a by nano-measurer software. Figure 10b depicts the statistical distribution of grain size and its Gaussian fitting. From Figure 10b, we can see that the grain size mainly ranges from 2.25 to 4.25 μm, and the average grain size is around 3.25 μm.

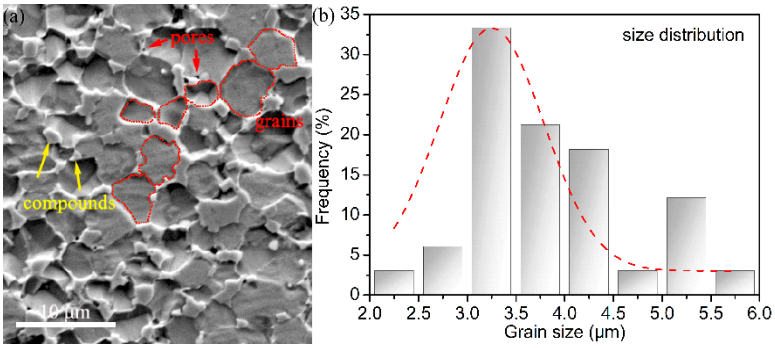

Figure 10. (**a**) SEM image of the bulk $(W_{35}Ta_{35}Mo_{15}Nb_{15})_{95}Ni_5$ RHEA after etching, (**b**) grain size distribution of HEA matrix.

3.3. Mechanical Properties

Compression test was performed at room temperature. Figure 11 shows the engineering compression stress–strain curve for the $(W_{35}Ta_{35}Mo_{15}Nb_{15})_{95}Ni_5$ RHEA. The compressive mechanical property of the bulk $(W_{35}Ta_{35}Mo_{15}Nb_{15})_{95}Ni_5$ RHEA and typical refractory HEAs reported were summarized in Table 1. In contrast with other typical RHEAs, the $(W_{35}Ta_{35}Mo_{15}Nb_{15})_{95}Ni_5$ RHEA possesses the advantages of both high strength and high fracture strain. It is necessary to take the microstructure and crystal structure of each phase into account to analyze the factors of the outstanding mechanical properties for the $(W_{35}Ta_{35}Mo_{15}Nb_{15})_{95}Ni_5$ RHEA. Firstly, solid solution strengthening is an intrinsic concept of HEAs on account of a severe lattice distortion [2]. Furthermore, unlike the typical as-casted RHEAs that have larger coarse-grains (grain size: 50–100 μm) [21], the as-sintered $(W_{35}Ta_{35}Mo_{15}Nb_{15})_{95}Ni_5$ RHEA displays a much finer and more homogeneous microstructure (grain size was approximately 3.25 μm), implying that grain boundary strengthening play a dominant part in the strength improvement. Grain boundary strengthening mechanism is described by the Hall–Petch formula ($\Delta\sigma_{gb} = k_y/\sqrt{d}$, where k_y is the Hall–Petch coefficient and d is the average grain size). In addition, it should be noted that the $(W_{35}Ta_{35}Mo_{15}Nb_{15})_{95}Ni_5$ RHEA in this study has marginal volume fraction of oxide inclusion phases $Nb_{5.7}Ni_4Ta_{2.3}O_2$ which contribute to the precipitation strengthening. Generally, precipitation strengthening mechanism complies with Orowan dislocation bypass mechanism or dislocation shearing mechanism. Given the two mechanisms traits, the high shear modulus and hardness of the oxide inclusion, Orowan dislocation bypass mechanism is more appropriate to assess the contribution of precipitate-reinforce mechanism. Finally, it is inevitable that interstitial elements such as O, N, C, etc, are introduced during the MA and SPS process, which contributes to interstitial solid solution strengthening [22]. Figure 11b,c depict compressive fracture morphologies of the $(W_{35}Ta_{35}Mo_{15}Nb_{15})_{95}Ni_5$ RHEA at room temperature. We can deduce that the compressive fracture mode is cleavage fracture from the fracture morphologies present a mixture of river-like pattern and steps.

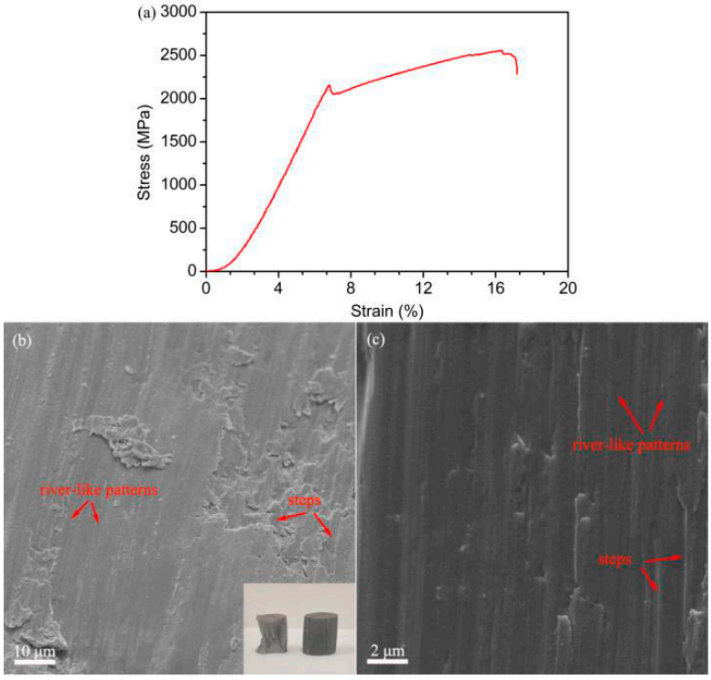

Figure 11. (**a**) Engineering stress–strain curve of the bulk $(W_{35}Ta_{35}Mo_{15}Nb_{15})_{95}Ni_5$ RHEA at room temperature, (**b**) fracture surface morphology and inserted compression sample image and (**c**) magnified fracture morphology.

Table 1. Compressive mechanical properties of typical RHEAs at room temperature.

Alloy	Process	Phase	$\sigma_{0.2}$(MPa)	σ_{max}(MPa)	ε_f(%)	Refs.
$(W_{35}Ta_{35}Mo_{15}Nb_{15})_{95}Ni_5$	MA+SPS (1700 °C)	bcc	~2128	~2562	8.16	This study
WTaMoNb	Arc melting	bcc	1058	1211	1.5	[10]
WTaMoNbV	Arc melting	bcc	1246	1270	1.7	[10]
WTaMoRe	Arc melting	bcc	-	1451	5.69	[23]
WTaMoNb	SPS	bcc	1217	1499	3.8	[24]
$WTaMoNbSi_{0.25}$	SPS	bcc	1826	2548	10.5	[24]
$WTaMoNbSi_{0.5}$	SPS	bcc	1883	2454	5.8	[24]

To sum up, the as-sintered $(W_{35}Ta_{35}Mo_{15}Nb_{15})_{95}Ni_5$ RHEA may be regarded as a potential candidate for high temperature structural material with high density and outstanding compressive strength owing to a combination of the four strengthening mechanisms.

4. Conclusions

A novel high strength $(W_{35}Ta_{35}Mo_{15}Nb_{15})_{95}Ni_5$ RHEA with high density was successfully fabricated by MA and SPS process in this study. The 12 h-milled powders with an average crystalline size of about 16.3 nm exhibit a single bcc solution phase. After the SPS process at 1700 °C, the bulk RHEA has a relative density of exceeding 96% and the average grain size is 3.25 μm. Meanwhile, minor oxide inclusion ($Nb_{5.7}Ni_4Ta_{2.3}O_2$) are detected in the bulk sample. The compressive yield stress, maximum stress and fracture strain of the $(W_{35}Ta_{35}Mo_{15}Nb_{15})_{95}Ni_5$ RHEA are 2128 MPa, 2562 MPa and 8.16%, respectively, which are superior to some typical RHEAs. The extraordinary high mechanical properties are attributed to the following factors: solid solution strengthening due to a severe lattice distortion, which is an intrinsic concept of HEAs, grain boundary strengthening, precipitation strengthening mechanism by second phases.

Author Contributions: Investigation, B.D. and Y.Y.; methodology, D.W.; project administration, X.L.; writing—original draft, Y.Y.; writing—review & editing, Z.W. All authors have read and agreed to the published version of the manuscript.

Funding: This research was supported by the Natural Science Foundation of Hunan Province, China (No. 2018JJ3677).

Conflicts of Interest: The authors declare that they have no known competing financial interests or personal relationships that could have appeared to influence the work reported in this paper.

References

1. Leek, H.; Chas, I.; Ryuh, J.; Hong, S.H. Effect of two-stage sintering process on microstructure and mechanical properties of ODS tungsten heavy alloy. *Mater. Sci. Eng. A* **2007**, *458*, 323–329.
2. Zhang, Y.; Yang, X.; Liaw, P.K. Alloy Design and Properties Optimization of High-Entropy Alloys. *JOM* **2012**, *64*, 830–838. [CrossRef]
3. Senkovo, N.; Miracled, B.; Chaputk, J. Development and exploration of refractory high entropy alloys—A review. *J. Mater. Res.* **2018**, *33*, 3092–3128. [CrossRef]
4. Li, Z.; Pradeep, K.G.; Deng, Y.; Raabe, D.; Tasan, C.C. Metastable high-entropy dual phase alloys overcome the strength-ductility trade-off. *Nature* **2016**, *534*, 227–230. [CrossRef] [PubMed]
5. Li, B.S.; Wang, Y.P.; Ren, M.X.; Yang, C.; Fu, H.Z. Effects of Mn, Ti and V on the microstructure and properties of AlCrFeCoNiCu high entropy alloy. *Mater. Sci. Eng. A* **2008**, *498*, 482–486. [CrossRef]
6. Wang, G.; Liu, Q.; Yang, J.; Li, X.; Sui, X.; Gu, Y.; Liu, Y. Synthesis and thermal stability of a nanocrystalline MoNbTaTiV refractory high-entropy alloy via mechanical alloying. *Int. J. Refract. Met. Hard Mater.* **2019**, *84*, 104988. [CrossRef]
7. Long, Y.; Liang, X.; Su, K.; Peng, H.; Li, X. A fine-grained NbMoTaWVCr refractory high-entropy alloy with ultra-high strength: Microstructural evolution and mechanical properties. *J. Alloy Compd.* **2019**, *780*, 607–617. [CrossRef]
8. Liu, Y.; Lu, Y.; Zhang, Y.; Miao, W. Study of nickel's effect on the synthesis of TiC during mechanical alloying. *Powder Metall. Technol.* **2007**, *25*, 96–98. (In Chinese)
9. Kang, B.; Lee, J.; Ryu, H.J.; Hong, S.H. Ultra-high strength WNbMoTaV high-entropy alloys with fine grain structure fabricated by powder metallurgical process. *Mater. Sci. Eng. A* **2018**, *712*, 616–624. [CrossRef]
10. Senkov, O.N.; Wilks, G.B.; Scott, J.M.; Miracle, D.B. Mechanical properties of Nb25Mo25Ta25W25 and V20Nb20Mo20Ta20W20 refractory high entropy alloys. *Intermetallics* **2011**, *19*, 698–706. [CrossRef]
11. Cullity, B.D.; Stock, S.R. *Elements of X-ray Diffraction*, 3rd ed.; Prentice Hall: Upper Saddle River, NJ, USA, 2001.
12. Chen, Y.L.; Hu, Y.H.; Hsieh, C.A.; Yeh, J.W.; Chen, S.K. Competition between elements during mechanical alloying in an octonary multi-principal-element alloy system. *J. Alloy Compd.* **2009**, *481*, 768–775. [CrossRef]
13. Ji, W.; Wang, W.; Wang, H.; Zhang, J.; Wang, Y.; Zhang, F.; Fu, Z. Alloying behavior and novel properties of CoCrFeNiMn high-entropy alloy fabricated by mechanical alloying and spark plasma sintering. *Intermetallics* **2015**, *56*, 24–27. [CrossRef]
14. Zak, A.K.; Majid, W.A.; Abrishami, M.E.; Yousefi, R. X-ray analysis of ZnO nanoparticles by WilliamsoneHall and sizeestrain plot methods. *Solid State Sci.* **2011**, *13*, 251–256.
15. Williamson, G.K.; Hall, G.K. X-ray line broadening from filed aluminium and wolfram. *Acta Metall.* **1953**, *1*, 22–31. [CrossRef]
16. Williamson, G.K.; Smallman, R.E. Dislocation densities in some annealed and cold-worked metals from measurements on the X-ray debye-scherrer spectrum. *Philos. Mag.* **1956**, *1*, 34–46. [CrossRef]
17. Schliephake, D.; Medvede, A.E.; Imran, M.K.; Obert, S.; Fabijanic, D.; Heilmaier, M.; Molotinkov, A.; Wu, X.H. Precipitation behaviour and mechanical properties of a novel Al0.5MoTaTi complex concentrated alloy. *Scr. Mater.* **2019**, *173*, 16–20. [CrossRef]
18. Yeh, J.W.; Chen, S.K.; Lin, S.J.; Gan, J.Y.; Chin, T.S.; Shun, T.T.; Tsau, C.H.; Chan, G.S.Y. Nanostructured high-entropy alloys with multiple principle elements: Novel alloy design concepts and outcomes. *Adv. Eng. Mater.* **2004**, *6*, 299–303. [CrossRef]
19. Yang, X.; Zhang, Y. Prediction of high-entropy stabilized solid-solution in multi-component alloys. *Mater. Chem. Phys.* **2012**, *132*, 233–238. [CrossRef]

20. Guo, S.; Ng, C.; Lu, J.; Liu, C.T. Effect of valence electron concentration on stability of fcc or bcc phase in high entropy alloys. *J. Appl. Phys.* **2011**, *109*, 645–647. [CrossRef]
21. Lv, S.; Zu, Y.; Chen, G.; Fu, X.; Zhou, W. An ultra-high strength CrMoNbWTi-C high entropy alloy co-strengthened by dispersed refractory IM and UHTC phases. *J. Alloy Compd.* **2018**, *788*, 1256–1264. [CrossRef]
22. Long, Y.; Zhang, H.; Wang, T.; Huang, X.; Li, Y.; Wu, J.; Chen, H. High-strength Ti–6Al–4V with ultrafine-grained structure fabricated by high energy ball milling and spark plasma sintering. *Mater. Sci. Eng. A* **2013**, *585*, 408–414. [CrossRef]
23. Wei, Q.; Shen, Q.; Zhang, J.; Chen, B.; Luo, G.; Zhang, L. Microstructure and mechanical property of a novel ReMoTaW high-entropy alloy with high density. *Int. J. Refract. Met. Hard Mater.* **2018**, *77*, 8–11. [CrossRef]
24. Guo, Z.; Zhang, A.; Han, J.; Meng, J. Effect of Si additions on microstructure and mechanical properties of refractory NbTaWMo high-entropy alloys. *J. Mater. Sci.* **2019**, *54*, 5844–5851. [CrossRef]